Production and transport of long lifetime excited states in pre-equilibrium ion solid collisions

Emily Lamour, Benoit Gervais, Jean Pierre Rozet, Dominique Vernhet

TABLES

TABLE I. Respective contribution of direct and cascade population to the total population for different nℓ states and two target thickness. The direct contribution corresponds to the population at the exit of the foil. The cascade contribution corresponds to the population coming from upper levels by radiative decay behind the foil.

	3.5 µg/cm^2 target		98 µg/cm^2 target	
$n\ell$ state	% direct	% cascade	% direct	% cascade
2p	60	40	51	49
2s	74	26	84	16
3p	89	11	86	14
4p	≈ 100		99	1

TABLE II. Energy of each observed line with the associated efficiency and global transmission for one of the Si(Li) detector. The efficiency of the other Si(Li) detector corresponds to 70% of the values given here. E_{Proj} and E_{Lab} correspond respectively to energies in the projectile and laboratory frames. Energies of the Lyman line are taken from Ref[23]. "*" marks energy of the centre of the theoretical distribution of the 2E1 decay mode Ref [22].

Observed Lines	Energy (eV)		Si(Li) detector	
	E_{Proj}	E_{Lab} (θ_L=90°)	Efficiency	$T^{n\ell}_{glob}$
Lyα	3321	3273	0.83 (±7%)	8.62 10^{-6} (±9.5%)
Lyβ	3936	3879	0.88 (±7%)	9.20 10^{-6} (±9.5%)
Lyγ	4150	4091	0.90 (±7%)	9.36 10^{-6} (±9.5%)
$\sum_5^\infty(np \rightarrow 1s)$	4362	4299	0.91 (±7%)	9.50 10^{-6} (±9.5%)
2E1	1660*	1636*	0.39 (±8%)	4.01 10^{-6} (±10.5%)

FIGURES CAPTIONS

FIG. 1. Schematic representation of the experimental set-up. Effects leading to X-ray auto-absorption are displayed in a zoom (see text).

FIG. 2. Energy distribution of the 2E1 decay mode for an Ar^{17+} ion: the theoretical distribution (dotted line), the distribution corrected by the Si(Li) detector efficiency alone (dashed line) and the "experimental" distribution (solid line) i.e. the distribution corrected by the efficiency convoluted with the detector resolution. Si(Li) detector efficiency is also plotted (dash-dotted line) for sake of clarity.

FIG. 3. Spectra recorded by a Si(Li) detector after backgrounds subtraction at various ion time of flight (delay time) behind the 3.5 µg/cm^2 carbon target: (a) t = 0; (b) t = 108 ps; (c) t = 600 ps.

FIG. 4. Normalized evolution of the Lyman lines emission (see text) as a function of the distance behind the target: experimental data (symbols: ● target of 3.5 µg/cm^2, ■ 8.6 µg/cm^2, □ 98 µg/cm^2 and ○ 201 µg/cm^2), binary ion-atom conditions i.e. including cascade contribution without any transport effects accounted for (dotted curves), classical transport "wake off" (solid curves: target of 3.5 µg/cm^2, dashed dotted curves: 201 µg/cm^2). The real distance *d* behind the target has been arbitrary shifted by 0.55 mm to clarify the graph.

FIG. 5. Slope evolution of the delayed Lyman line intensities versus foil thickness; circles with error bars: experiment (symbols with error bars); classical transport (triangles); fit with a decay function given in the text (solid lines). The a_{3p} has been divided by 2 to clarify the graph.

FIG. 6. Evolution with the time of flight of the Ar^{17+} Lyman line intensities (i.e. number of emitted photon per ion) for the 3.5 µg/cm^2 carbon target: experimental results (symbols), classical transport model "wake off" (solid black lines) and "wake on" (solid grey lines), rate equation model (dashed lines). In the simulations, the CDW calculations have been used to account for the primary capture processes. The distance behind the target has been arbitrary shifted by 0.55 mm for sake of clarity.

FIG. 7. Same as Fig. 6 for the 8.6 µg/cm^2 target thickness.

FIG. 8. Same as Fig. 6 for the 12.6 µg/cm^2 target thickness.

FIG. 9. Same as Fig. 6 for the 42 µg/cm^2 target thickness.

FIG. 10. Same as Fig. 6 for the 98 µg/cm^2 target thickness.

FIG. 11. Absolute $2s_{1/2}$ populations of Ar^{17+} at $v_p = 23$ a.u. impact velocity as a function of carbon target thickness: experimental data (symbols); binary ion-atom

conditions i.e. including cascade contribution without any transport effects accounted for (dotted black curve); classical transport model "wake off" (solid black line) and "wake on" (solid grey line); rate equations model (dashed black line); Master equations model with complete CDW calculations to describe the initial capture process (dashed grey line) and Master equations model with CDW calculations and with the phases of coherences of the initial states taken equal to zero (dash-dot-dotted grey line).

FIG. 12. Geometrical efficiency function of Si(Li) detectors for $z \geq 0.87$; z is the position of the target support and Z the position where $n\ell \rightarrow 1s$ transitions are recorded.

FIG. 13. Geometrical efficiency function of Si(Li) detectors for $0.55 \leq z \leq 0.87$; z is the position of the target support and Z the position where $n\ell \rightarrow 1s$ transitions are recorded. The hatched area is hidden by the support.

FIG. 14. Geometrical efficiency function of Si(Li) detectors for $0.25 + e \leq z \leq 0.55$; z is the position of the target support and Z the position where $n\ell \rightarrow 1s$ transitions are recorded. The parameters e and $\delta(z)$ are defined in the text. The hatched area is hidden by the support.

FIG. 15. Geometrical efficiency function of Si(Li) detectors for $-0.07 + e' \leq z \leq 0.25 + e$; z is the position of the target support and Z the position where $n\ell \rightarrow 1s$ transitions

are recorded. The parameters e, e' and $\delta(z)$ are defined in the text. The hatched area is hidden by the support.

FIG. 16. Geometrical efficiency function of Si(Li) detectors for $0.25 \leq z \leq 0.87$; z is the position of the target support and Z the position where $n\ell \rightarrow 1s$ transitions are recorded. The hatched area is hidden by the support.

FIG. 1. Schematic representation of the experimental set-up. Effects leading to X-ray auto-absorption are displayed in a zoom (see text).

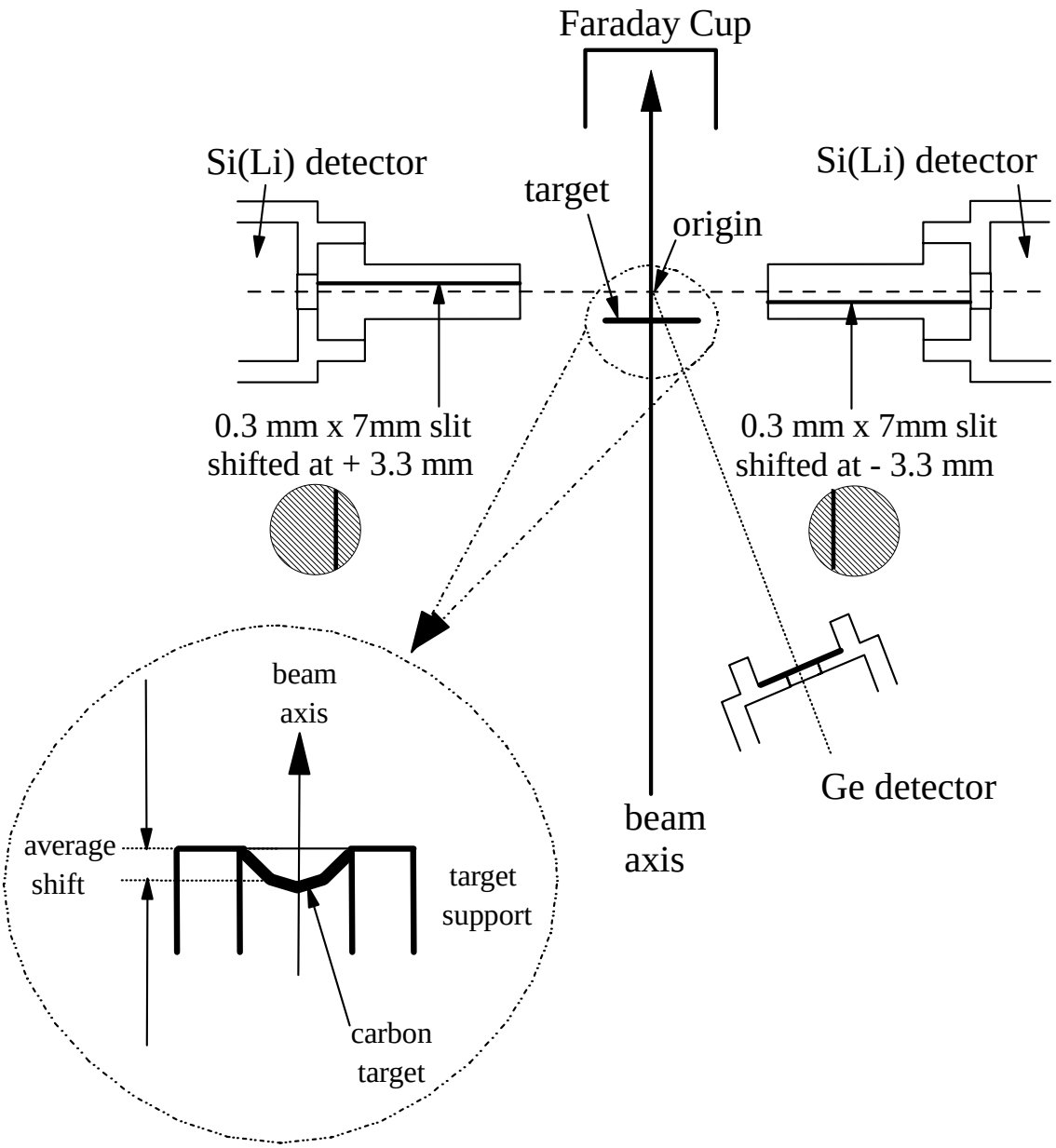

FIG. 2. Energy distribution of the 2E1 decay mode for an Ar^{17+} ion: the theoretical distribution (dotted line), the distribution corrected by the Si(Li) detector efficiency alone (dashed line) and the "experimental" distribution (solid line) i.e. the distribution corrected by the efficiency convoluted with the detector resolution. Si(Li) detector efficiency is also plotted (dash-dotted line) for sake of clarity.

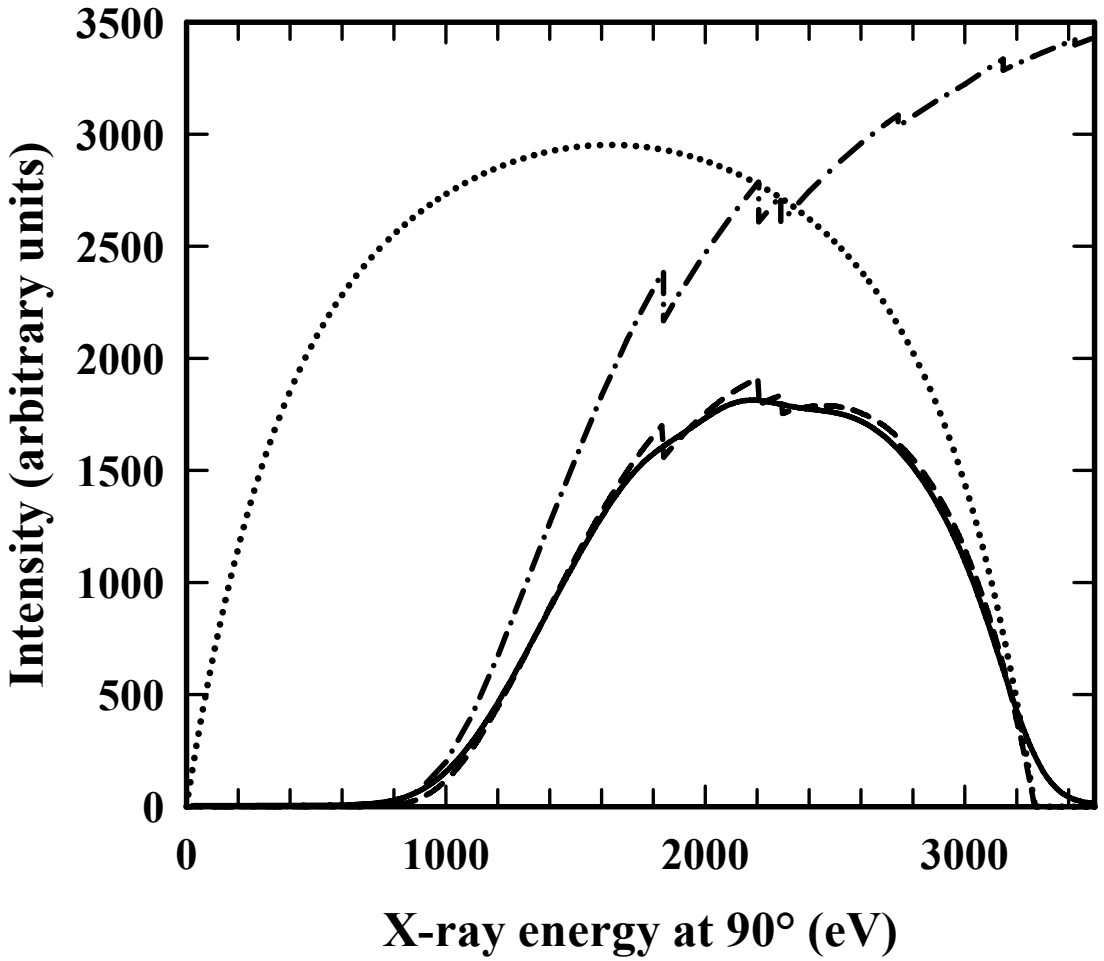

FIG. 3. Spectra recorded by a Si(Li) detector after backgrounds subtraction at various ion time of flight (delay time) behind the 3.5 μg/cm^2 carbon target: (a) t = 0; (b) t = 108 ps; (c) t = 600 ps.

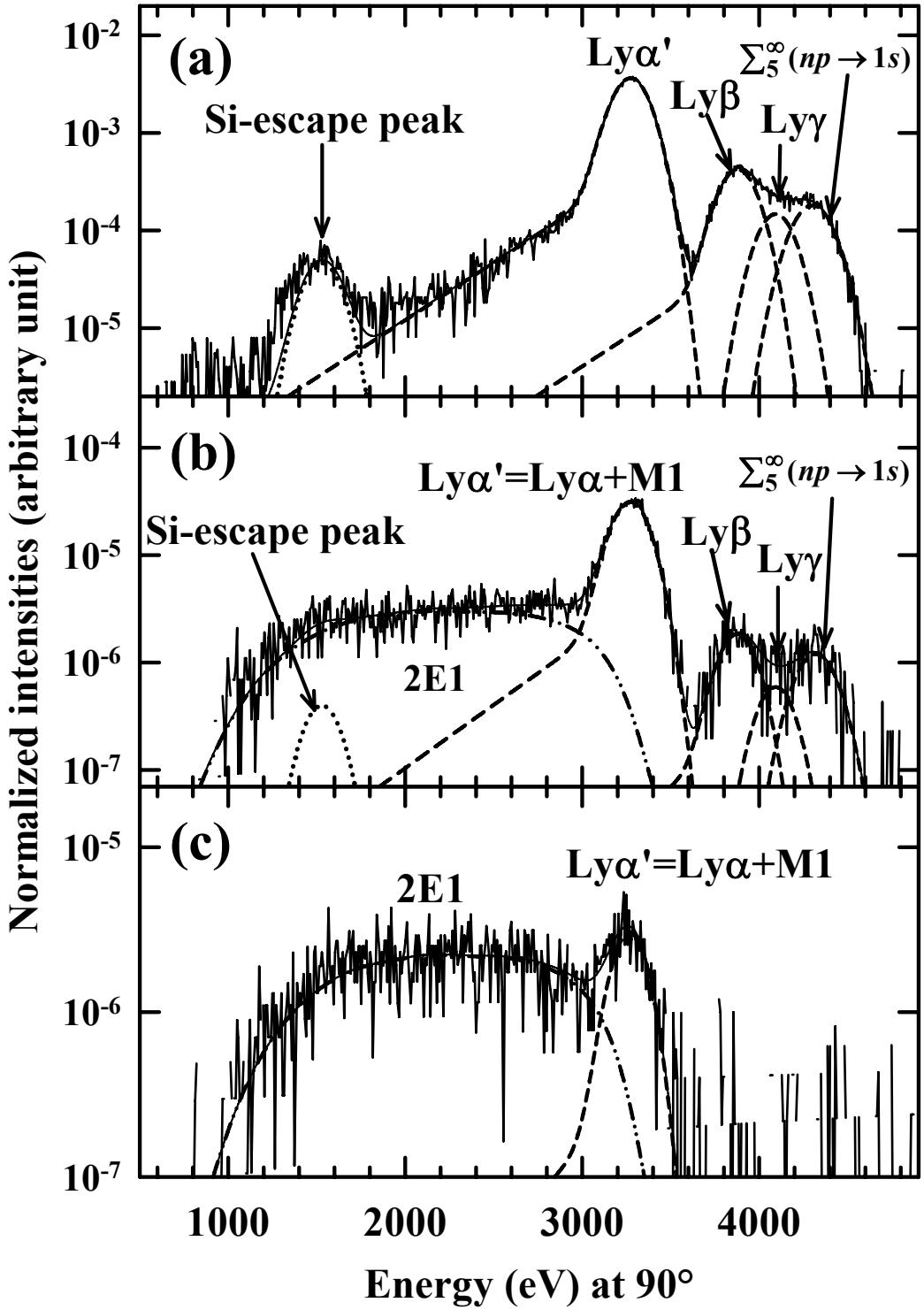

FIG. 4. Normalized evolution of the Lyman lines emission (see text) as a function of the distance behind the target: experimental data (symbols: ● target of 3.5 µg/cm^2, ■ 8.6 µg/cm^2, □ 98 µg/cm^2 and ○ 201 µg/cm^2), binary ion-atom conditions i.e. including cascade contribution without any transport effects accounted for (dotted curves), classical transport "wake off" (solid curves: target of 3.5 µg/cm^2, dashed dotted curves: 201 µg/cm^2). The real distance *d* behind the target has been arbitrary shifted by 0.55 mm to clarify the graph.

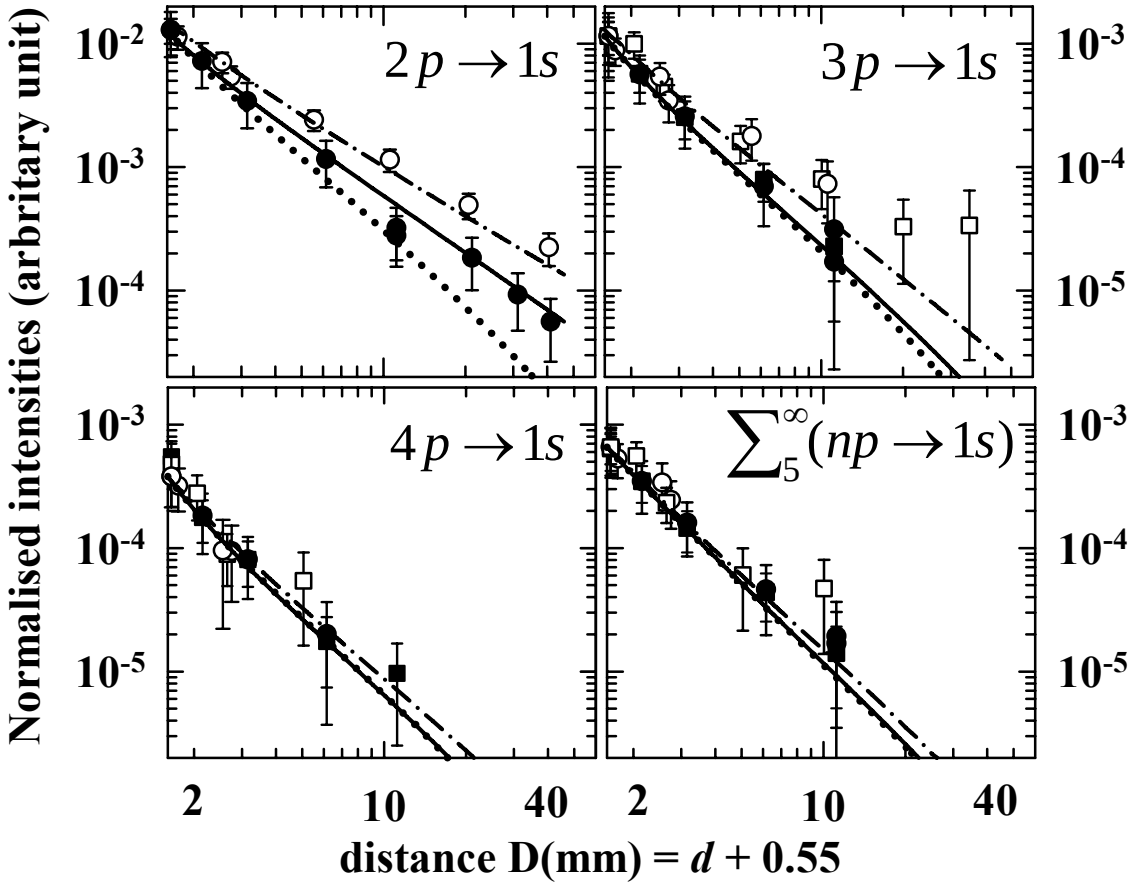

FIG. 5. Slope evolution of the delayed Lyman line intensities versus foil thickness; circles with error bars: experiment (symbols with error bars); classical transport (triangles); fit with a decay function given in the text (solid lines). The a_{3p} has been divided by 2 to clarify the graph.

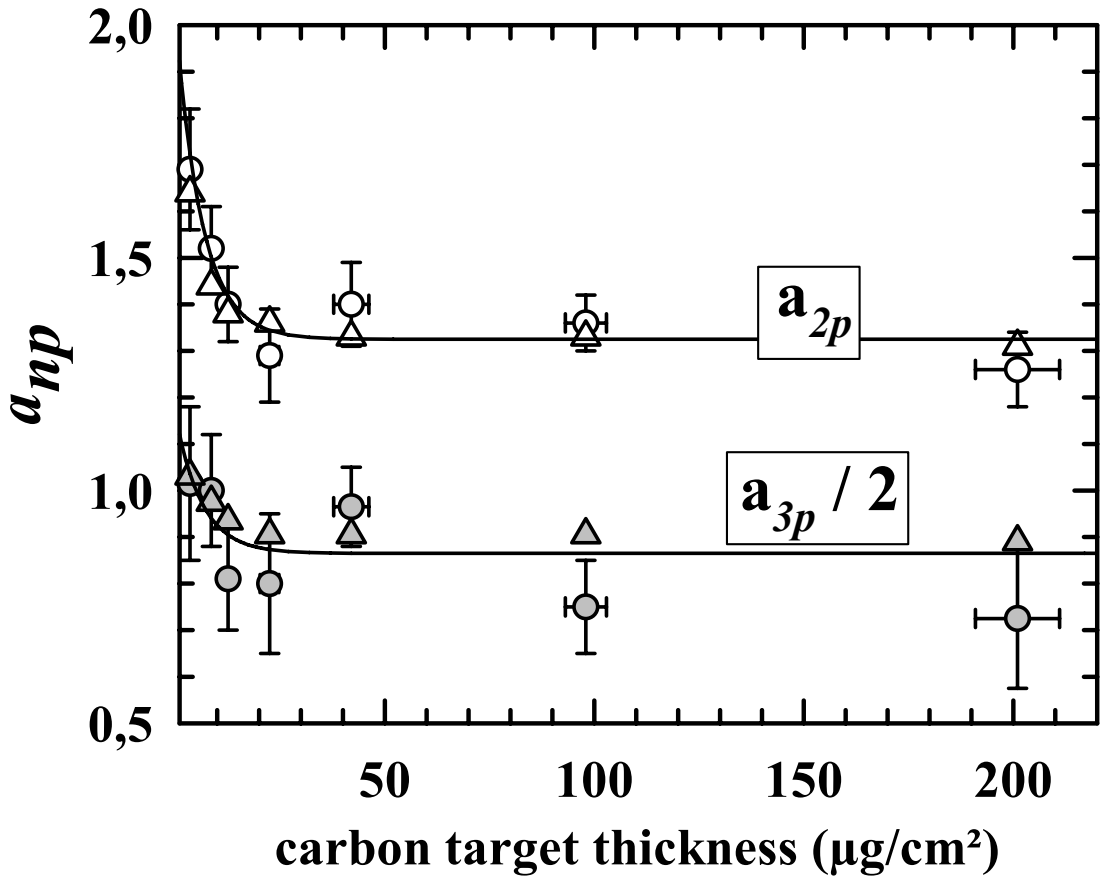

FIG. 6. Evolution with the time of flight of the Ar^{17+} Lyman line intensities (i.e. number of emitted photon per ion) for the 3.5 µg/cm^2 carbon target: experimental results (symbols), classical transport model "wake off" (solid black lines) and "wake on" (solid grey lines), rate equation model (dashed lines). In the simulations, the CDW calculations have been used to account for the primary capture processes. The distance behind the target has been arbitrary shifted by 0.55 mm for sake of clarity.

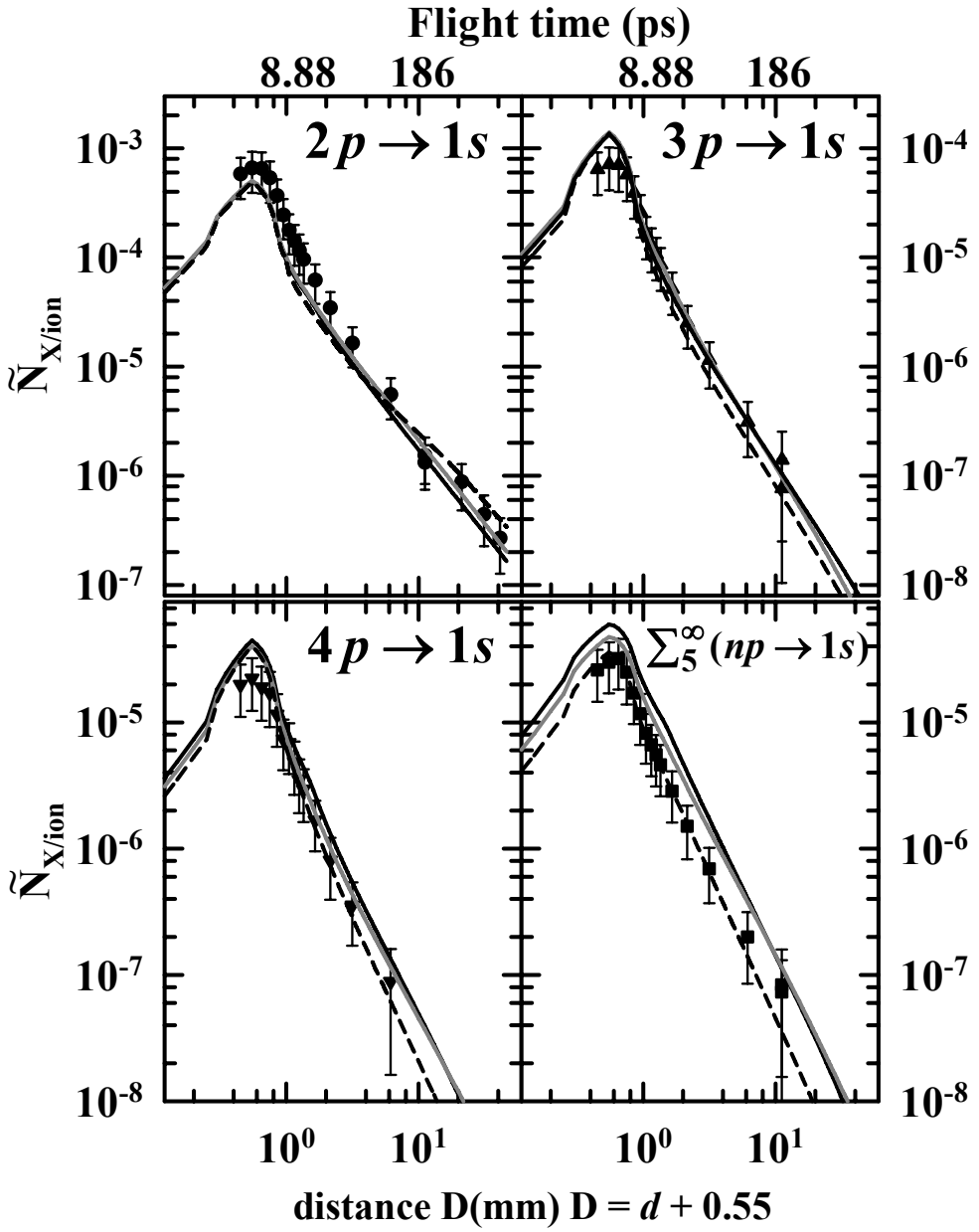

FIG. 7. Same as Fig. 6 for the 8.6 μg/cm^2 target thickness.

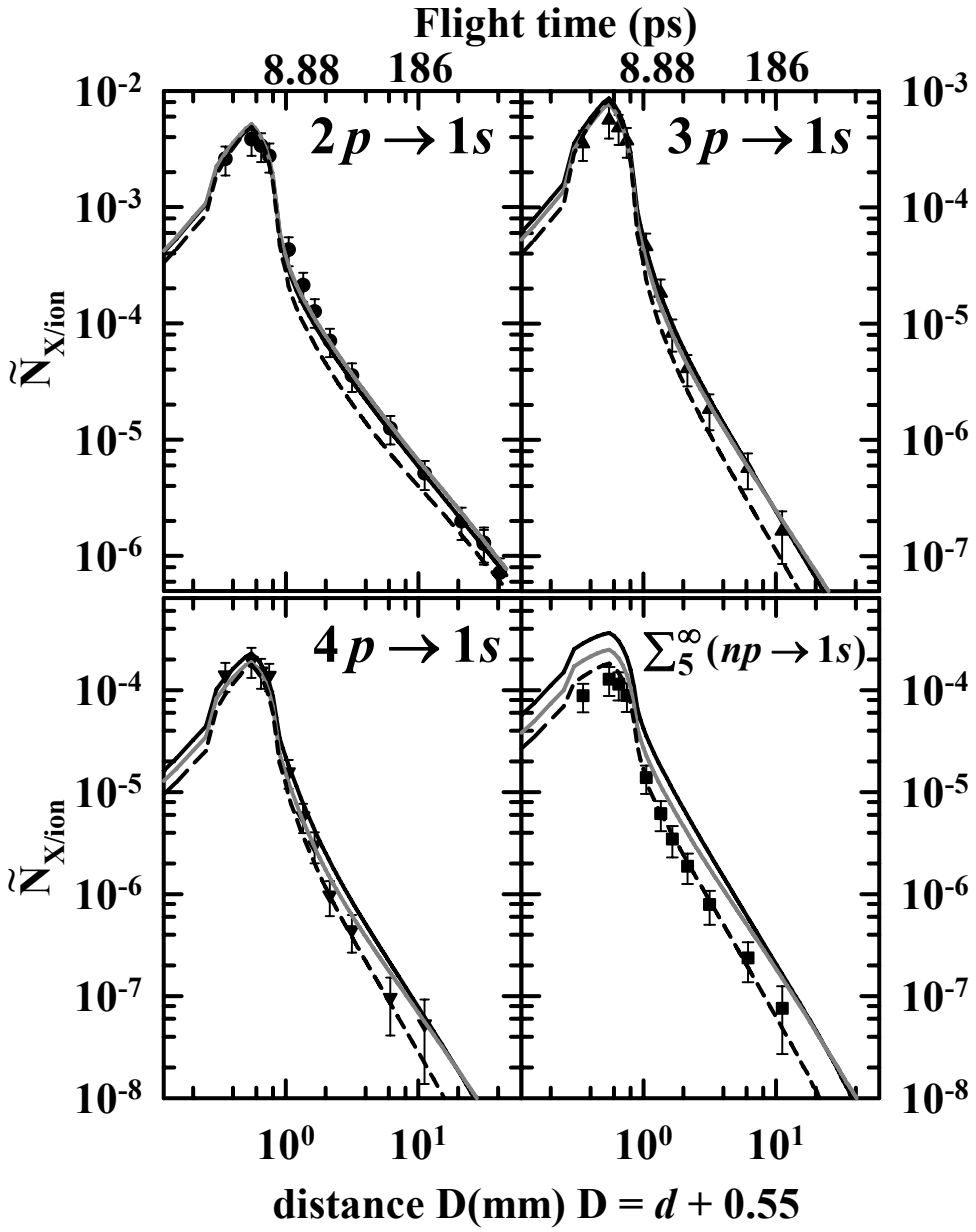

FIG. 8. Same as Fig. 6 for the 12.6 μg/cm^2 target thickness.

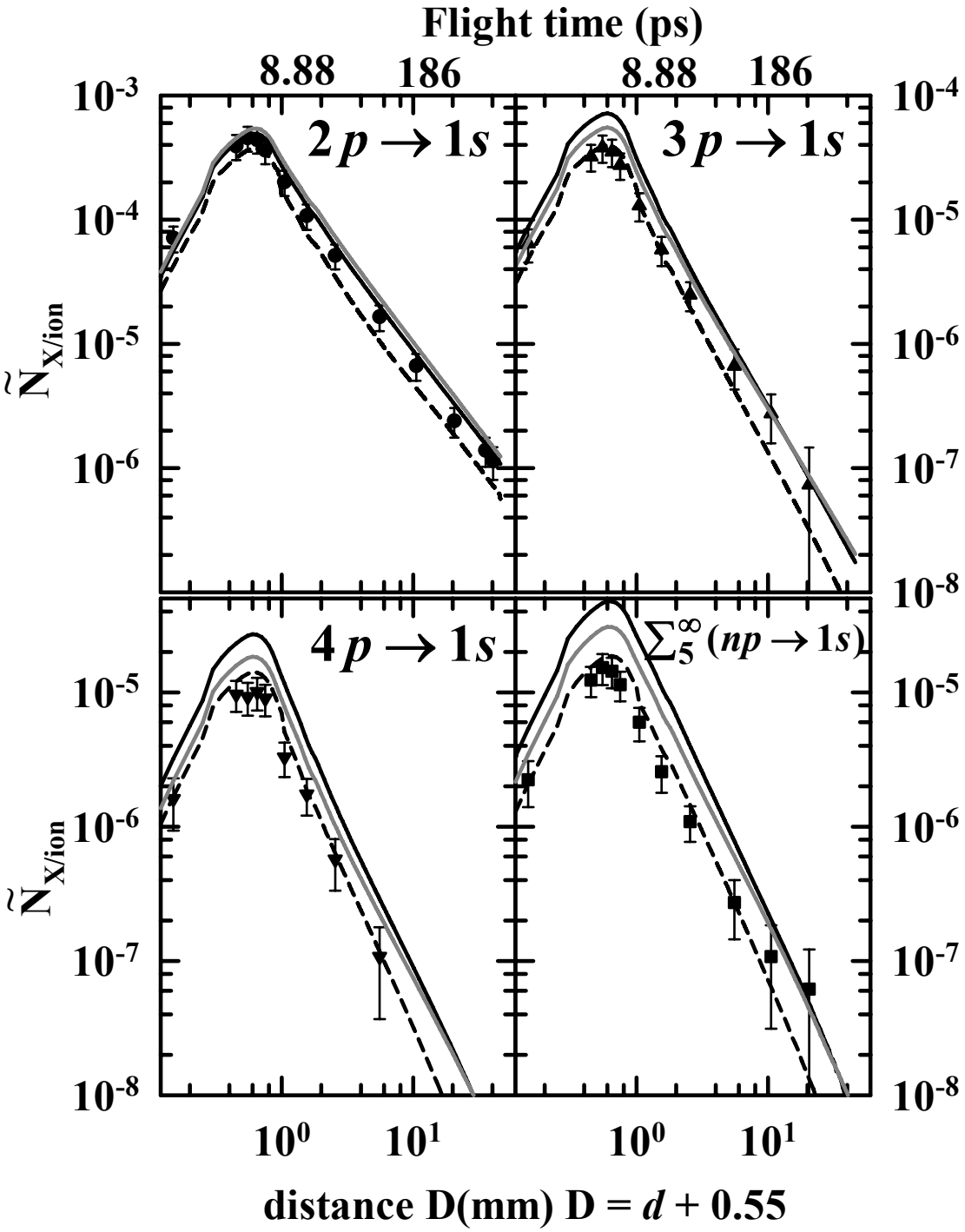

FIG. 9. Same as Fig. 6 for the 42 μg/cm2 target thickness.

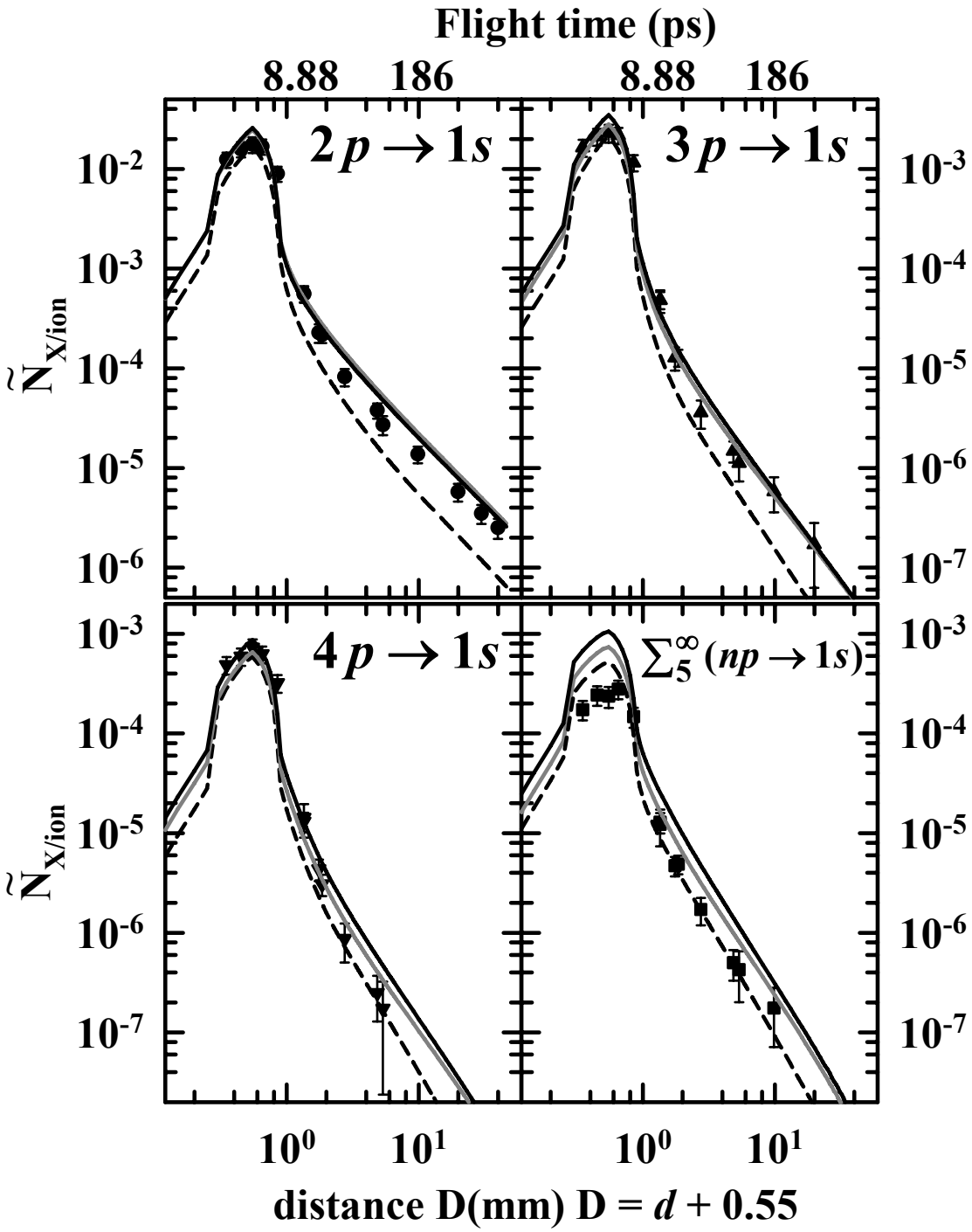

FIG. 10. Same as Fig. 6 for the 98 μg/cm2 target thickness.

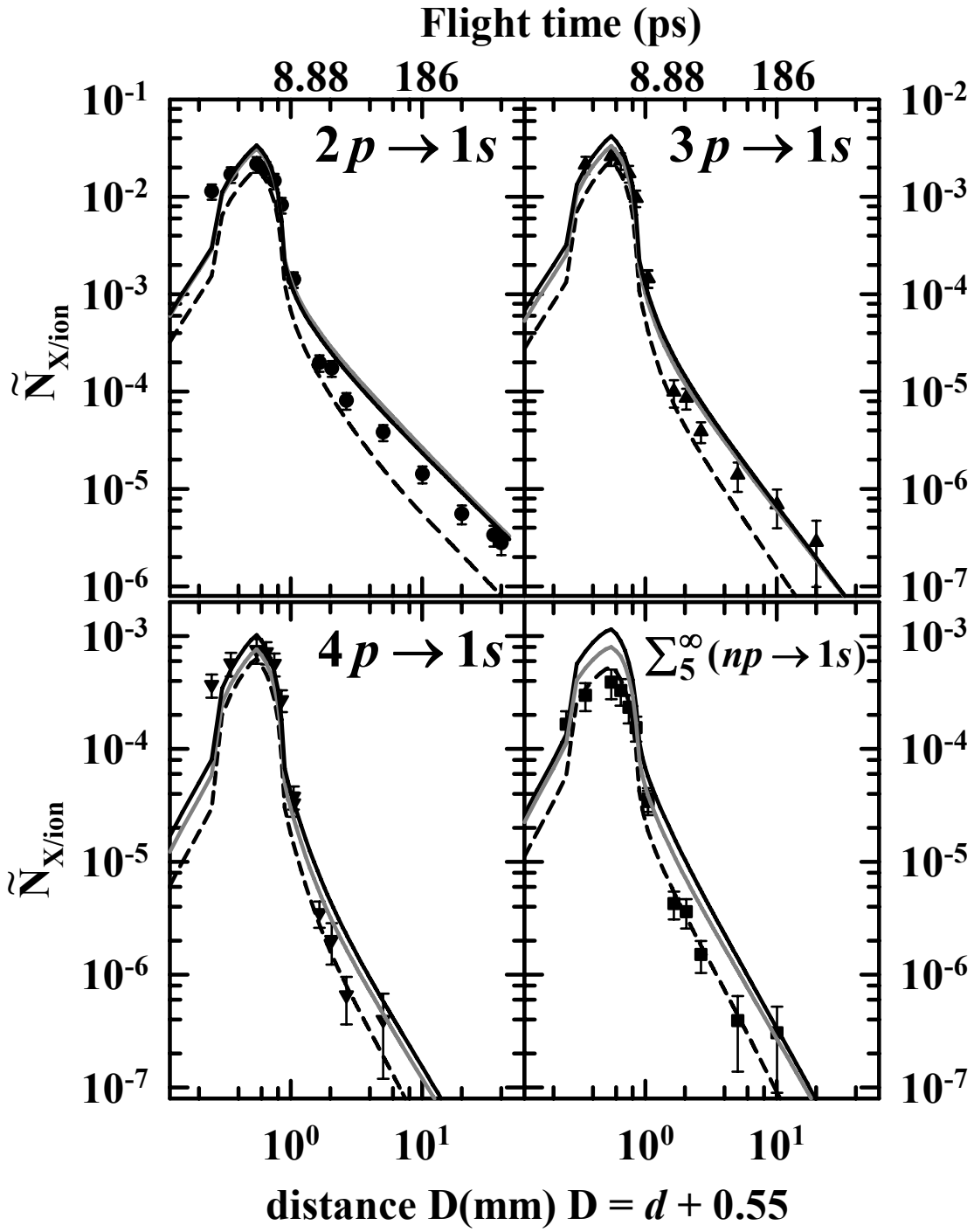

FIG. 11. Absolute $2s_{1/2}$ populations of Ar^{17+} at v_p = 23 a.u. impact velocity as a function of carbon target thickness: experimental data (symbols); binary ion-atom conditions i.e. including cascade contribution without any transport effects accounted for (dotted black curve); classical transport model "wake off" (solid black line) and "wake on" (solid grey line); rate equations model (dashed black line); Master equations model with complete CDW calculations to describe the initial capture process (dashed grey line) and Master equations model with CDW calculations and with the phases of coherences of the initial states taken equal to zero (dash-dot-dotted grey line).

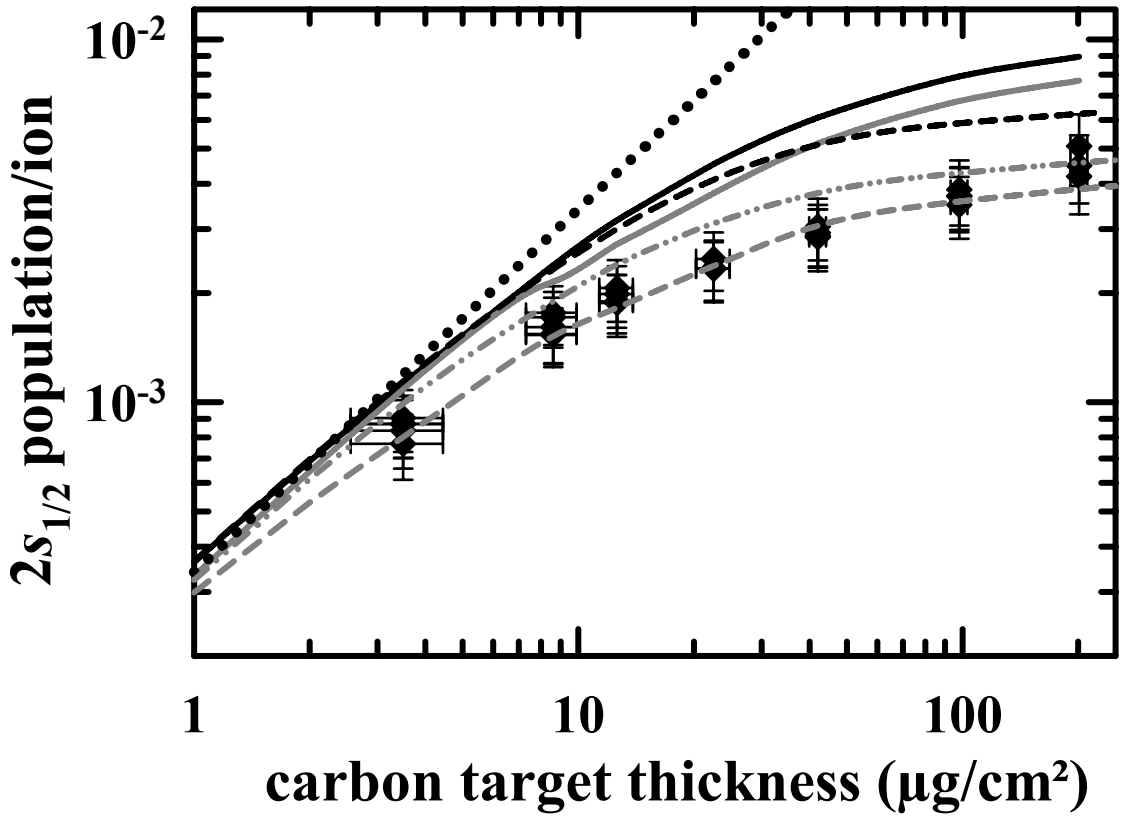

FIG. 12. Geometrical efficiency function of Si(Li) detectors for $z \geq 0.87$; z is the position of the target support and Z the position where n$\ell \rightarrow$ 1s transitions are recorded.

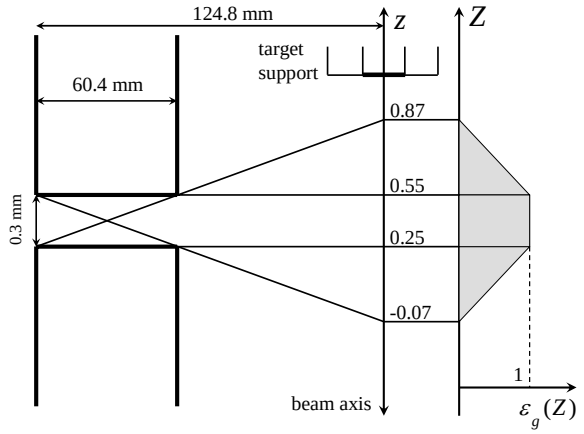

FIG. 13. Geometrical efficiency function of Si(Li) detectors for $0.55 \leq z \leq 0.87$; z is the position of the target support and Z the position where $n\ell \rightarrow 1s$ transitions are recorded. The hatched area is hidden by the support.

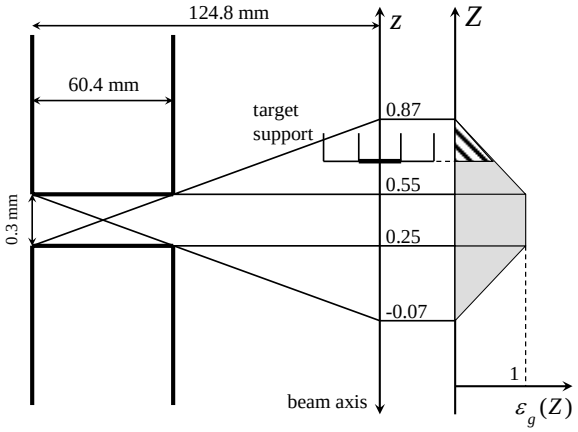

FIG. 14. Geometrical efficiency function of Si(Li) detectors for 0.25 + e ≤ z ≤ 0.55; z is the position of the target support and Z the position where n$\ell \rightarrow$ 1s transitions are recorded. The parameters e and $\delta(z)$ are defined in the text. The hatched area is hidden by the support.

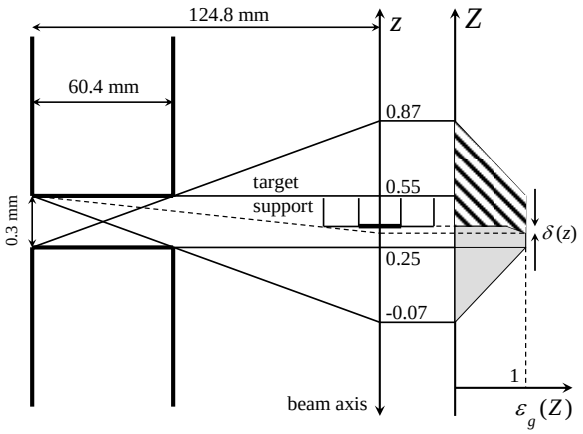

FIG. 15. Geometrical efficiency function of Si(Li) detectors for - 0.07 + e' ≤ z≤ 0.25 + e; z is the position of the target support and Z the position where $n\ell \rightarrow 1s$ transitions are recorded. The parameters e, e' and $\delta(z)$ are defined in the text. The hatched area is hidden by the support.

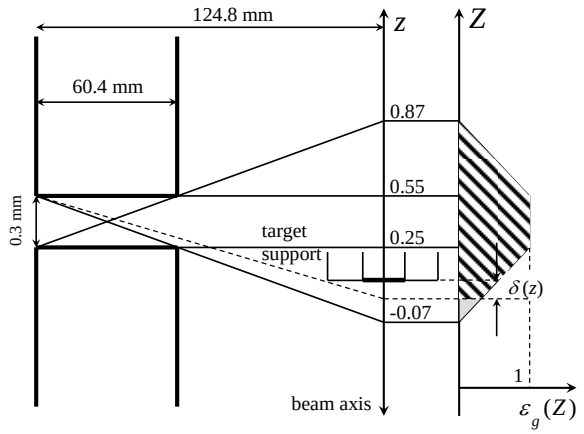

FIG. 16. Geometrical efficiency function of Si(Li) detectors for $0.25 \leq z \leq 0.87$; *z is the position of the target support and Z* the position where $n\ell \rightarrow 1s$ transitions are recorded. The hatched area is hidden by the support.